



# Gradient-based enhancement of tubular structures in medical images



Rodrigo Moreno<sup>a,b,c,\*</sup>, Örjan Smedby<sup>a,b,c</sup>

<sup>a</sup> School of Technology and Health, KTH Royal Institute of Technology, Sweden

<sup>b</sup> Center for Medical Image Science and Visualization (CMIV), Linköping University, Sweden

<sup>c</sup> Department of Radiology and Department of Medical and Health Sciences (IMH), Linköping University, Sweden

## ARTICLE INFO

### Article history:

Received 12 October 2014

Revised 18 May 2015

Accepted 6 July 2015

Available online 29 July 2015

### Keywords:

Vesselness

Structure tensor

Spherical harmonics

## ABSTRACT

Vesselness filters aim at enhancing tubular structures in medical images. The most popular vesselness filters are based on eigenanalyses of the Hessian matrix computed at different scales. However, Hessian-based methods have well-known limitations, most of them related to the use of second order derivatives. In this paper, we propose an alternative strategy in which ring-like patterns are sought in the local orientation distribution of the gradient. The method takes advantage of symmetry properties of ring-like patterns in the spherical harmonics domain. For bright vessels, gradients not pointing towards the center are filtered out from every local neighborhood in a first step. The opposite criterion is used for dark vessels. Afterwards, structuredness, evenness and uniformness measurements are computed from the power spectrum in spherical harmonics of both the original and the half-zeroed orientation distribution of the gradient. Finally, the features are combined into a single vesselness measurement. Alternatively, a structure tensor that is suitable for vesselness can be estimated before the analysis in spherical harmonics. The two proposed methods are called Ring Pattern Detector (RPD) and Filtered Structure Tensor (FST) respectively. Experimental results with computed tomography angiography data show that the proposed filters perform better compared to the state-of-the-art.

© 2015 Elsevier B.V. All rights reserved.

## 1. Introduction

Several important anatomical structures in the human body have a tubular shape, including blood vessels, airways in the lungs and structures of the nervous and digestive system. Imaging and analyzing these structures is important for diagnostic purposes. As an example, computer tomography angiography (CTA) is now a standard clinical tool for diagnosing coronary artery diseases (Marwan et al., 2014; Weustink and de Feyter, 2011) and pulmonary embolism (Hogg et al., 2006; Mos et al., 2009). Magnetic resonance angiography (MRA) is used clinically for imaging the cerebral vessels (Parker et al., 1998) as well as the renal and peripheral arteries (Dong et al., 1999; Prince et al., 1999).

Both CTA and MRA use contrast agents in order to increase the visibility of vessels with respect to surrounding tissue. This increased contrast has allowed physicians to perform a better assessment in the clinic. Despite this, the level of contrast might not be enough for performing automatic analyses. One reason for this is that adjacent structures to vessels can also be enhanced by contrast agents, which

is for example the case of the heart chambers in coronary artery imaging. Another problem in patients is impeded flow of the contrast agent in diseased vessels, which results in lack of contrast in those areas. Additional issues include noise and low resolution, which can become a big hindrance for resolving small vessels. For these reasons, the automatic analysis of tubular structures from images acquired through CTA or MRA is still challenging.

In general, methods aiming at enhancing tubular structures in medical images are referred to as vesselness filters. These filters are useful in many medical image analysis applications. For example, some vessel segmentation methods include preprocessing steps for enhancing the vessels on images acquired through computed tomography or magnetic resonance angiography (CTA or MRA) in order to improve their results (cf. Lesage et al. (2009); Rudyanto et al. (2014) for a description of methods that follow this approach). Moreover, some state-of-the-art centerline extraction algorithms are also based on vesselness measurements (e.g., Yang et al., 2012; Schaap et al., 2009). From a clinical perspective, vesselness filters are also appealing, since they could be used for obtaining high quality images at low radiation doses in CTA.

An ideal vesselness filter should comply with at least the following requirements: both vessels and bifurcations should be enhanced, “bright” and “dark” vessels should be distinguished and the measurement should be scale- and rotation-invariant. In addition, more

\* Corresponding author at: School of Technology and Health, KTH Royal Institute of Technology, Sweden. Tel.: +46 700950675.

E-mail addresses: [rodrigo.moreno@sth.kth.se](mailto:rodrigo.moreno@sth.kth.se) (R. Moreno), [orjan.smedby@sth.kth.se](mailto:orjan.smedby@sth.kth.se) (Ö. Smedby).

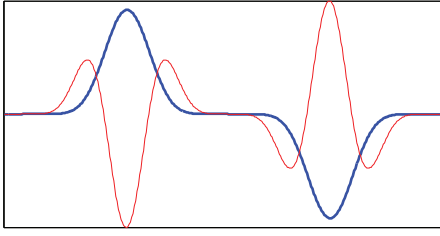


**Fig. 1.** Synthetic model of a 1D bright followed by a dark vessel (in blue) and the corresponding second order derivative (in red). The second order derivative can have peaks not only at the middle of the vessels but also at other locations. (For interpretation of the references to color in this figure legend, the reader is referred to the web version of this article.)

advanced requirements for an ideal filter include distinguishing between vessels and bifurcations, centerline delineation and vessel segmentation.

The most popular vesselness filters are based on the Hessian (Frangi et al., 1998; Li et al., 2003; Sato et al., 1998; Xiao et al., 2011; 2013; Yang et al., 2014). These methods take advantage of the fact that ideal bright vessels have negative (positive) peaks on the second derivative across of “bright” (“dark”) vessels and such a derivative is almost null along the vessel. These methods combine the eigenvalues of the Hessian at multiple scales into a single vesselness measurement.

For example, the method proposed by Frangi et al. (1998) computes vesselness as:

$$V_i = \left[ 1 - e^{-\frac{R_A^2}{2\alpha^2}} \right] e^{-\frac{R_B^2}{2\beta^2}} \left[ 1 - e^{-\frac{S^2}{2c^2}} \right] \quad (1)$$

or  $V_i = 0$  if  $\lambda_1 > 0$  or  $\lambda_2 > 0$ , where  $|\lambda_1| \geq |\lambda_2| \geq |\lambda_3|$  are the eigenvalues of the Hessian at the scale  $i$ ,  $\alpha$ ,  $\beta$  and  $c$  are parameters,  $S$  is the Frobenius norm of the Hessian, and  $R_A$  and  $R_B$  are computed as:

$$R_A = \frac{|\lambda_2|}{|\lambda_1|} \quad (2)$$

$$R_B = \frac{|\lambda_3|}{\sqrt{|\lambda_2\lambda_1|}} \quad (3)$$

Finally, the method computes vesselness as the maximum  $V_i$  estimated at different scales  $i$ .

Despite its success, the use of second order derivatives makes the Hessian-based vesselness filters very sensitive to overshooting artifacts. This problem can be better understood through the 1D example of Fig. 1. Assume, without loss of generality, that one is interested in bright vessels. Then, positive peaks of the second order derivative can safely be discarded. However, if not treated carefully, the negative peaks of the second order derivative that are not related to vessel peaks can easily lead to artifacts as shown in the figure. In higher dimensions, the second order derivative in all possible directions is encoded within the Hessian matrix. It is not difficult to show that the overshooting problem in 1D also affects the Hessian in higher dimensions. As in the 1D case, positive eigenvalues of the Hessian can safely be discarded for bright vessels. However, the Hessian can have negative eigenvalues at locations not related to vessels peaks, which can lead to errors in the vesselness estimation. Related to the Hessian, vesselness methods based on the analysis of the shape operator (also known as Weingarten map) have also been proposed (Armande et al., 1996; Prinnet et al., 1996). Unfortunately, these methods require not only second but also first order derivatives. Thus, the aforementioned problems also affect these methods. A different approach estimates the Hessian as the gradient of the regularized gradient field (Bauer and Bischof, 2008), where such a regularization is

performed through gradient vector flow (Xu and Prince, 1998). However, this method also requires second order derivatives.

In the last few years, alternative vesselness measurements have been proposed to tackle the problems of using second order derivatives. A first family of such methods estimates vesselness from an analysis on the gradient field. An interesting approach is based on the analysis of the flux of the gradient on the surface of local spheres (Vasilevskiy and Siddiqi, 2002). The main hypothesis of the method is that such a flux attains its maximum at the centerline of the vessels. Efficient implementations of this method have been proposed (Law and Chung, 2009). This approach has been extended to oriented variants with reported better results than the original non-oriented approach (Benmansour and Cohen, 2011; Law and Chung, 2008; Law et al., 2012, 2013; Xiao et al., 2013).

A different method that uses the gradient analyzes the eigendecomposition of the gradient structure tensor (GST) in order to enhance vessel-like structures (Agam et al., 2005; Agam and Wu, 2005). Linked to this approach, Wiemker et al. (2013) use a modified version of the GST for vesselness estimation. This approach is discussed in detail in Section 2 since it is very related to the method we propose in that section.

Intensity values have also been used for vesselness estimation. Moments of the intensity values have been used as an alternative to the Hessian (Hernández Hoyos et al., 2006; Nemitz et al., 2007). These methods could have difficulties in regions with strong adjacent structures, such as the heart chambers. Similar to that approach, Cetin et al. (2013) compute tensors from the intensity values, which can be analyzed for detecting vessel-like structures. Moreover, Qian et al. (2009) use patterns of the intensity profile for vesselness estimation. Also, model-fitting of the intensity profiles have been proposed (Friman et al., 2010; Würz and Rohr, 2007).

Another family of methods uses a bank of oriented filters that combined can yield a probability map that can be used for vesselness (Auvray et al., 2009). A very related approach is the use of orientation scores (Hannink et al., 2014). Furthermore, diffusion filtering have been used for enhancing vessels, e.g. Cañero and Radeva (2003); Krissian (2002); Manniesing et al. (2006). Unfortunately, these last-mentioned methods rely on the estimation of the Hessian at different scales.

More recently, alternative machine learning techniques based on features of the image intensity and gradient (Zheng et al., 2011, 2012) have also been proposed as alternatives to Hessian-based methods. Indeed, the performance of these methods depends on the adequacy of the training data with respect to the application, and on the set of features used in the computations.

An approach related to the method proposed in Section 3 is the one by Rivest-Hénault and Cheriet (2013). This method analyzes second order derivative distributions through spherical harmonics at different scales. Unlike that method, our approach is not exposed to the problems of using second order derivatives and, on top of that, it is able to analyze multiple scales by performing all the computations at a single scale. The reader is referred to review papers for a more extensive list of approaches, e.g., Lesage et al. (2009) or Kirbas and Quek (2004).

In this paper, we propose two methods for determining vesselness using the gradient. At an intermediate step, a modified version of the GST, which is suitable for vesselness estimation, is introduced. We refer to this method as filtered structure tensor (FST). Building on top of this approach, the proposed method analyzes the spherical harmonics expansion of the local orientation distribution of the gradient, which is more appropriate than the FST for analyzing vessels with bifurcations. Since this method looks for ring patterns in the local orientation distribution, we refer to this method as ring pattern detector (RPD).

The paper is organized as follows. Section 2 proposes the modified version of the GST for vesselness estimation (FST). Section 3 describes

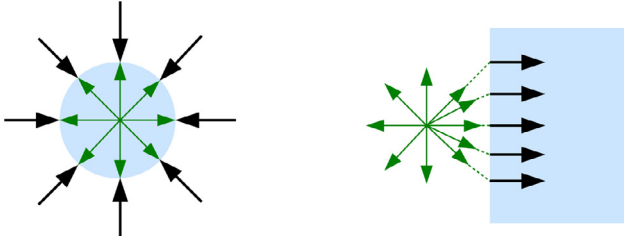


**Fig. 2.** Strategy followed by Wiemker et al. (2013) for weighting the gradients. A radial function  $\hat{r}$  (in green) is used to weight the gradients (in black) in a neighborhood of a point. Left: the point is located at the center of a bright vessel. Right: the point is outside a bright structure. (For interpretation of the references to color in this figure legend, the reader is referred to the web version of this article.)

the proposed method based on the spherical harmonics expansions (RPD). Section 4 shows the results of the conducted experiments. Finally, Section 5 discusses the results and makes some final remarks.

## 2. Filtered structure tensor

The method proposed in this section is based on a modification of the original GST, which is given by (Förstner, 1986):

$$T(\vec{x}) = G * \nabla I \nabla I^T, \quad (4)$$

where  $G$  is a Gaussian kernel,  $I$  is the image and “ $*$ ” is the convolution operation.

It is clear that the GST is not a good candidate for vesselness estimations. The direction of the gradient is lost by applying the dyadic product in (4) making it unable to distinguish between dark and bright vessels. Moreover, gradients from nearby tissue can interfere on the GST, so the tensors can become more anisotropic than they should at vessels.

In order to solve this problem, Wiemker et al. (2013) proposed the so-called radial structure tensor (RST), which can be written as:

$$T_w(\vec{x}) = \sum_{\vec{x}' \in N(\vec{x})} \alpha(\vec{x}, \vec{x}') (\nabla I(\vec{x}') \circ \hat{r}(\vec{x}')^T) \quad (5)$$

where  $\hat{r}(\vec{x}') = \frac{\vec{x}' - \vec{x}}{|\vec{x}' - \vec{x}|}$  is a normalized radial function, “ $\circ$ ” is the Jordan product and  $\alpha(\vec{x}, \vec{x}')$  is a function of the integral of the intensities between the origin  $\vec{x}$  and the neighbor  $\vec{x}'$ . Once the tensor is computed, a vesselness measurement can be obtained by combining its eigenvalues, similarly to the Hessian-based approaches.

In (5),  $\hat{r}$  acts through the Jordan product as a weighting function of the importance of the gradient in the computations. Fig. 2 shows this strategy. Notice that this idea is closely related to the optimally oriented flux approach (Benmansour and Cohen, 2011; Law and Chung, 2008; Xiao et al., 2013). An appealing feature of this method is that, unlike Hessian-based approaches, it performs all computations at a single scale. In general, this tensor is able to detect vessels with a scale lower or equal than a given one, since it considers all gradients in the neighborhood.

One problem of this strategy is that the Jordan product also gives value to gradients coming from adjacent structures, which can lead to inaccuracies. Thus, the effectiveness of this method mainly relies on the function  $\alpha$ . However, the function  $\alpha$  is computationally expensive and it can have problems dealing with small vessels.

Indeed, the expensive computation of  $\alpha$  can be avoided by using an appropriate operator on the gradient. In particular, instead of using  $\hat{r}$  to weight the gradient, we propose to use it to filter out the gradients that are not likely part of the vessel. Thus, we propose the following structure tensor:

$$FST(\vec{x}) = G * \nabla I' \nabla I'^T, \quad (6)$$

with  $I'$  being the filtered gradient, which is computed as:

$$\nabla I' = H(t \nabla I^T \vec{r}) \nabla I \quad (7)$$

where  $H$  is the Heaviside function,  $\vec{r} = \vec{x}' - \vec{x}$  and  $t$  takes its value depending on the type of vessel of interest:  $t = -1$  for bright and  $t = 1$  for dark vessels. As an example, when  $t = -1$  the radial function is used to filter out the gradients not pointing towards the center of bright vessels. As in Wiemker et al. (2013), vesselness is computed by combining the eigenvalues of the proposed tensor following the methodology of Hessian-based approaches. In particular, (1) where the Hessian has been replaced by the computed structure tensors, has been used in the experiments for computing the vesselness measure for the methods described in this section. For similar reasons to the ones described for the method by Wiemker et al. (2013), it is sufficient to compute a single scale to obtain a vesselness measure.

The main advantage of the proposed structure tensor compared to previously proposed methods is that it is not affected by the previously discussed drawbacks of using second order derivatives and it is less sensitive to biases generated by gradients from nearby structures compared to the method proposed by Wiemker et al. (2013).

## 3. Ring pattern detector

Figs. 3 and 4 can be used to describe intuitively the principle of the proposed method in this section. For every specific point in the space, it is possible to translate the gradients from a local neighborhood to the origin of a unitary sphere. This mapping can be used to show the distribution of orientations of the gradient at a specific neighborhood, or equivalently, can be interpreted as the local angular histogram of the gradient in 3D. This mapping can be modeled as a function on the surface of the unitary sphere  $S^2$ , which will be referred to as the local orientation distribution of the gradient (LODG). This function can also be thought of as a local variant of the well-known extended Gaussian image (EGI) (Horn, 1984; Moreno et al., 2012b).

Let us first assume the case of noiseless vessel trees isolated from neighboring structures such as the heart chambers. Let us also assume that we are only interested in analyzing points located at centerlines.

As seen in Fig. 3, the gradients in vessels and bifurcations are perpendicular to the depicted rings (in red). These rings correspond to ring-like patterns in the LODG (see Fig. 4a–c). In other words, the gradient is

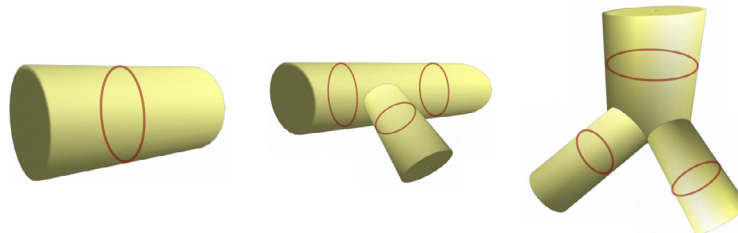


**Fig. 3.** Gradients in vessels and bifurcations are perpendicular to the depicted rings (in red). These rings correspond to ring-like patterns in the local orientation distribution of the gradient. (For interpretation of the references to color in this figure legend, the reader is referred to the web version of this article.)

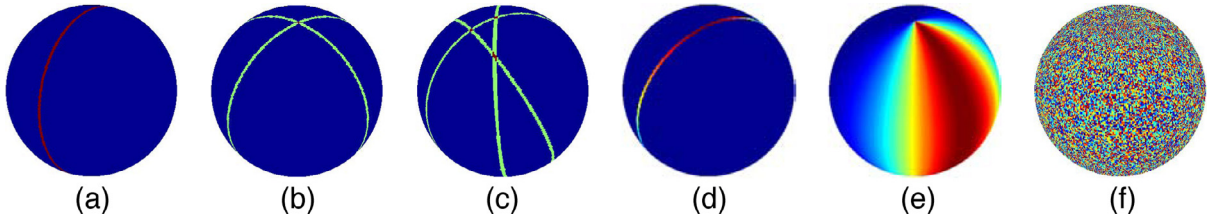


**Fig. 4.** Shape of the LODG at different locations. (a) LODG at the centerline of an idealized vessel. (b) LODG at a noiseless T-bifurcation. (c) LODG at a noiseless Y-bifurcation. (d) LODG at an idealized vessel but not at the centerline. (e) LODG at a location outside the vessels. (f) LODG at a noisy location outside the vessels.

distributed in great circles in the LODG both inside vessels and bifurcations. On the other hand, these ring-like patterns are not present at points outside the vessel tree (e.g. Fig. 4e). This means that the aforementioned structures of interest can potentially be characterized by the presence of ring-like patterns in the LODG.

Now we can consider more general cases. First, notice that the existence of ring-like patterns in the LODG is not affected by additive noise. This means that detectors of ring-like patterns in the LODG are potentially less sensitive to noise than other methods. As an example, notice that the structure tensor introduced in the previous section could face problems distinguishing between bifurcations (Fig. 4b and c) and noisy locations outside the vessels (Fig. 4f).

Second, consider points inside the vessels but not located at centerlines. Centerline extraction methods can benefit from vesselness filters that yield stronger signal at centerlines than at other locations inside the vessels. This feature can easily be addressed by weighting the gradients in the LODG with a radial Gaussian function. Although the LODG at the centerline and other locations will display ring-like patterns, the ones from points outside centerlines will become anisotropic (see Fig. 4d). Such a difference can be used to strengthen the signal at centerlines.

Finally, consider the presence of large neighboring structures, something that is common in images acquired from the coronary arteries. It is clear that gradients coming from those structures can distort the LODG. However, this problem can be tackled by using the filtered gradient  $\nabla I'$  computed through (7) instead of the original gradient for creating the LODG, as described in the previous section.

Notice that the structure tensor proposed in the previous section can be seen as a second order tensorial approximation of the LODG. However, such an approximation can be insufficient for detecting higher-order structures such as bifurcations and can be more sensitive to noise. The next subsection describes the proposed method more formally.

### 3.1. Feature estimation

As already mentioned, the goal of the method is to distinguish between functions with ring-like patterns and other functions on  $S^2$ . Our approach is to perform this task by detecting asymmetries of these functions. As shown in Edvardson and Smedby (2003), spherical harmonics are versatile for analyzing functions on  $S^2$ . In the same line, the proposed method makes use of spherical harmonics for detecting asymmetries related to non ring-like patterns.

A function  $f$  on  $S^2$  can be expanded in terms of spherical harmonics, also referred to as Laplace series, by:

$$f(\theta, \phi) = \sum_{\ell=0}^{\infty} \sum_{m=-\ell}^{\ell} A_{\ell}^m Y_{\ell}^m(\theta, \phi), \quad (8)$$

where  $\theta$  and  $\phi$  are the colatitude and azimuth coordinates respectively,  $Y_{\ell}^m$  is the spherical harmonics of degree  $\ell$  and order  $m$ , and  $A_{\ell}^m$  are computed as:

$$A_{\ell}^m = \int_{S^2} f(\theta, \phi) \bar{Y}_{\ell}^m(\theta, \phi) d\Omega \quad (9)$$

with  $\bar{Y}_{\ell}^m$  being the complex conjugate of  $Y_{\ell}^m$ .

The autocorrelation power spectrum in spherical harmonics, which can be computed for every degree  $\ell$  as:

$$P_{\ell} = \frac{1}{2\ell+1} \sum_{m=-\ell}^{\ell} |A_{\ell m}|^2 \quad (10)$$

is appealing for our purposes, since it is rotation-invariant.

Thanks to the symmetries of  $Y_{\ell}^m$ , it is easy to show that  $A_{\ell}^m = 0$ , and consequently  $P_{\ell} = 0$ , for  $\ell$  odd, when the function has antipodal symmetry. We take advantage of this fact for measuring the asymmetry of the LODG through the following two features:

$$E = \frac{\sum_{\ell=1}^{\infty} P_{2\ell}}{\sum_{\ell=1}^{\infty} P_{\ell}} \quad (11)$$

$$U = \frac{P_0}{\sum_{\ell=0}^{\infty} P_{\ell}} \quad (12)$$

On the one hand,  $E$  can be seen as an “evenness” measure whose value is reduced with the asymmetry of the LODG. On the other hand,  $U$  can be seen as a “uniformness” measure, whose value is maximum for the uniform distribution. Thus,  $E$  can be used to discard regions outside the vessels, while  $U$  can be used for distinguishing vessels and bifurcations from unstructured regions. Also notice that  $E$  does not consider  $P_0$ . Consequently, the estimation of  $E$  is insensitive to uncorrelated noise, which is related to an increase of  $P_0$ . However,  $E$  is still sensitive to ring patterns since, unlike uncorrelated noise, such patterns have non-null autocorrelation power spectra of even order higher than 0. Notice that  $E$  and  $U$  are scale-invariant since they are based on measuring asymmetries where the strength of the rings are largely disregarded.

In some regions, the contrast given by  $E$  and  $U$  may be insufficient for distinguishing rings from the uniform distribution in noisy scenarios. However, such differences can be enhanced by inducing asymmetries on the LODG. The idea behind this procedure is that such asymmetries will affect more the uniform distribution than ring-like patterns. The easiest way to induce asymmetries is to set to zero half of the LODG. Thus, two extra parameters,  $E_{1/2}$  and  $U_{1/2}$ , can be obtained by computing  $E$  and  $U$  on the half-zeroed LODG using (11) and (12).

In addition to  $E$ ,  $U$ ,  $E_{1/2}$  and  $U_{1/2}$ , a “structuredness” measure  $S$  can be obtained by summing up the power spectrum of all degrees:

$$S = \sum_{\ell=0}^{\infty} P_{\ell}. \quad (13)$$

This measurement can be used to disregard flat regions that are not likely part of the vessel network.

Similarly to the methods presented in Section 2, it is only necessary to perform the computations at a single scale, since the features are detected at any scale lower or equal than a given one. This is because these methods consider all gradients in a neighborhood, not only those that are at a certain radius. In the case that only a specific range of scales  $[\rho_1, \rho_2]$  is of interest, the proposed methods can easily



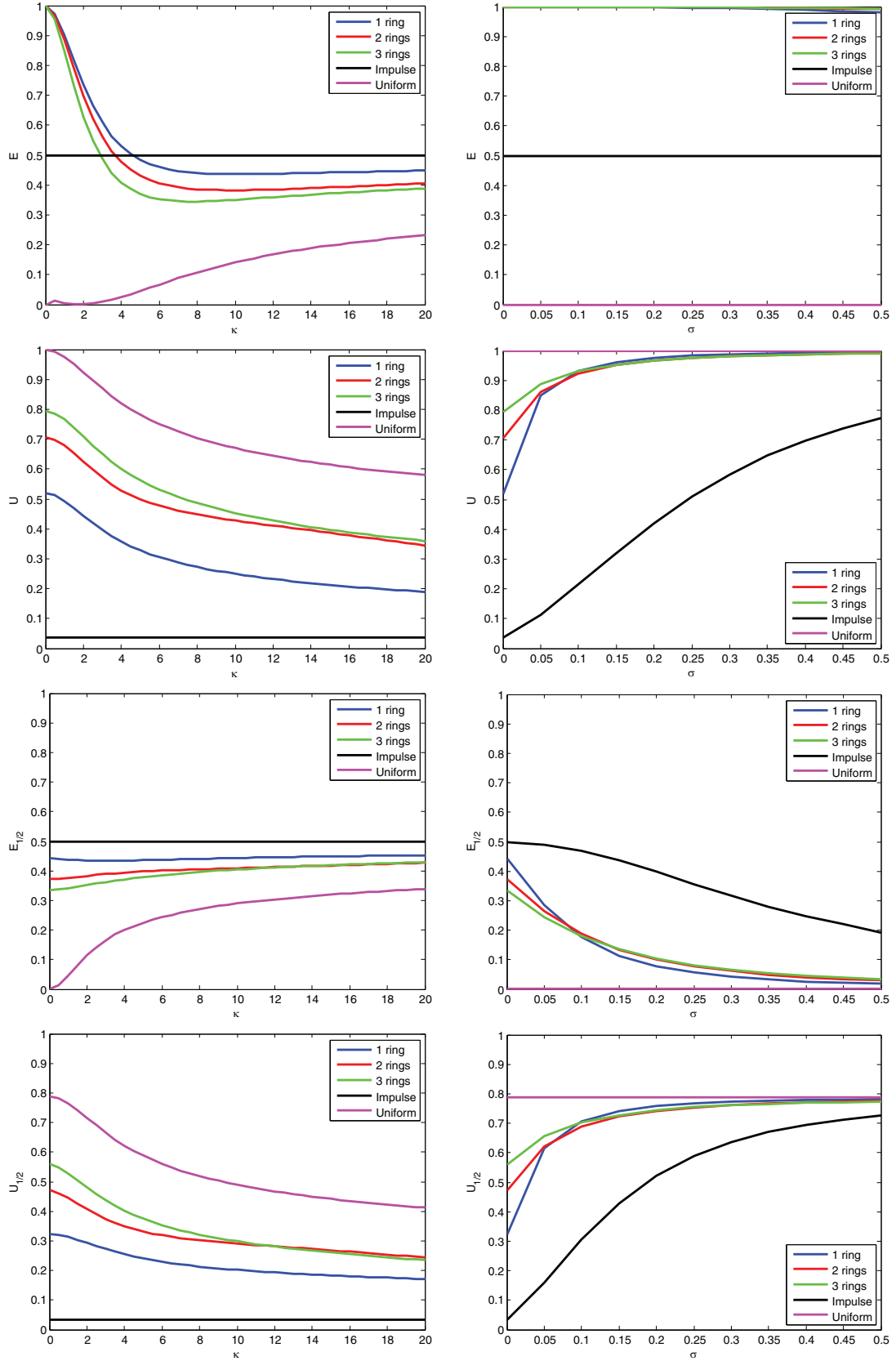
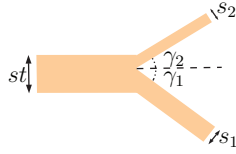


Fig. 5. Evolution of  $E$ ,  $U$ ,  $E_{1/2}$  and  $U_{1/2}$  with the degree of anisotropy (left) and with the amount of additive white Gaussian noise on the LODG (right) for 5 different cases.



**Fig. 6.** Synthetic Y-bifurcation for testing the sensitivity of the proposed measurements with respect to the relative scales of the branches  $s_1$  and  $s_2$  and to the angles between the branches and the trunk  $\gamma_1$  and  $\gamma_2$ . The scale of the trunk  $st$  has been set to one.

be adapted by using the function:

$$\tilde{r}(\vec{x}', \vec{x}) = \begin{cases} (\vec{x}' - \vec{x}), & \text{if } \|\vec{x}' - \vec{x}\| \in [\rho_1, \rho_2] \\ -t \nabla I, & \text{otherwise,} \end{cases} \quad (14)$$

instead of  $\tilde{r}$  in (7).

An implementation issue of the proposed method is to determine the degree  $L$  after which the Laplace series of (8) can be cut off. Basically,  $L$  depends on the complexity of the LODG. As an example, in CTA and MRA data, the most complex function of interest involves 3 rings, corresponding to a Y-bifurcation. Let us first consider locations at the centerlines. In such locations, due to antipodal symmetry, it is possible to approximate the LODG with higher order tensors of even order. As a rule of thumb, it is necessary to increment two orders to the tensors in order to resolve a new structure. This means that, resolving 3 rings will require at least 6th order tensors. Considering the one-to-one relationship between symmetrical function expansions in spherical harmonics of degree  $L$  and tensors of even order  $L$  (Özarslan and Mareci, 2003), it is safe to cut off the Laplace series in (8) at  $L = 6$  for CTA and MRA data.

### 3.2. Vesselness measurement

Once the five features proposed in the previous section are estimated, the next step is to combine them into a single vesselness

measurement. This section describes tests on synthetic data, whose aim is to provide the intuition for appropriately combining the features described above into a single vesselness measurement in order to make it appropriate for real data.

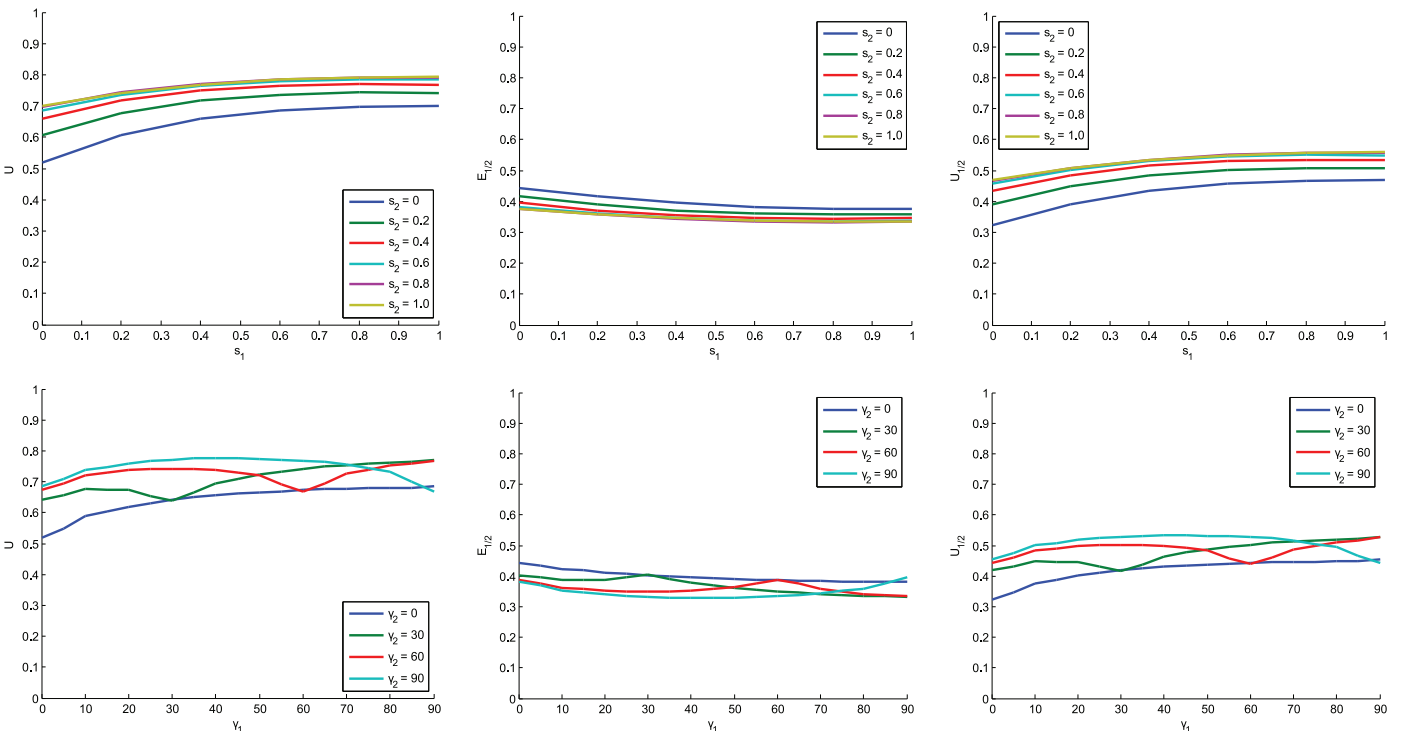
Five datasets have been considered in the tests: LODGs with 1–3 rings (cf. Fig. 4a–c), a LODG with an impulse function and the uniform distribution. The last two datasets have been included in the tests as extreme cases.

Fig. 5 shows the evolution of  $E$ ,  $U$ ,  $E_{1/2}$  and  $U_{1/2}$  with a simulated increase of anisotropy for different LODGs. Anisotropy has been simulated by weighting the original LODGs with the function  $\exp(\kappa \sin(\phi/2))$  with parameter  $\kappa$ . Moreover, this figure also shows the evolution of  $E$ ,  $U$ ,  $E_{1/2}$  and  $U_{1/2}$  with the increase of additive white Gaussian noise on the LODGs. As shown in the figure, it is not difficult to distinguish between ring-like patterns from impulse and uniform distributions, even in presence of strong anisotropies or large amounts of noise.

Fig. 6 shows the geometry of the Y-bifurcation used in the experiments summarized in Fig. 7. The top of this figure shows the evolution of  $U$ ,  $E_{1/2}$  and  $U_{1/2}$  for a Y-bifurcation where the scales of the branches have been set as fractions  $s_1$  and  $s_2$  of the scale of the main trunk.  $E$  is not shown in this figure, since it is always 1. As shown, the variability of these three parameters is relatively small, even for large differences in scale. That means that, in practice, the analysis of the LODG can be performed at a single scale, corresponding to the largest scale of the tubular structure of interest.

Regarding the angle between the rings, the bottom of Fig. 7 shows the evolution of  $U$ ,  $E_{1/2}$  and  $U_{1/2}$  for a planar Y-bifurcation with the angles  $\gamma_1$  and  $\gamma_2$  between the trunk and the two branches (cf. Fig. 6). As in the previous case,  $E$  is always 1. The low variability of the values with respect to the two angles means that they are robust to the angle between the trunk and its branches.

From Figs. 5 and 7, combining sigmoids seems appropriate for distinguishing ring patterns from other cases. Given the sigmoid



**Fig. 7.** Top: evolution of  $U$ ,  $E_{1/2}$  and  $U_{1/2}$  for a Y-bifurcation with the scales of the branches  $s_1$  and  $s_2$  with  $st = 1$  and  $\gamma_1 = \gamma_2 = \pi/4$ . Bottom: evolution of  $U$ ,  $E_{1/2}$  and  $U_{1/2}$  for a planar Y-bifurcation with the angles  $\gamma_1$  and  $\gamma_2$  (in degrees) between the trunk and the two branches with  $st = s_1 = s_2 = 1$ .

function:

$$\Gamma(x) = 1/(1 + \exp(-\beta x)) \quad (15)$$

with parameter  $\beta$  and function  $\hat{S}$  given by:

$$\hat{S} = 1 - \exp(-S^2/2s^2) \quad (16)$$

with parameter  $s$ , we propose the following vesselness measurement:

$$\text{RPD} = \Gamma(E - p_1) \Gamma(U - p_2) \Gamma(2E_{1/2} - p_3) \Gamma(U_{1/2} - p_4) \hat{S} \quad (17)$$

where  $p_1$  to  $p_4$  are parameters, and RPD stands for ring pattern detector. Notice that function  $\hat{S}$  was proposed by Frangi et al. (1998) for weighting their measurement of structuredness. However, this function is applied in the proposed method to the structuredness  $S$ , which is computed through (13).

Default values for parameters  $p_i$  for  $i \in [1, 4]$  required for computing the proposed vesselness measurement can be obtained by analyzing the results of Figs. 5 and 7. From these figures, it is easy to assess that good results can be expected by setting all  $p_i = 0.3$ . In turn, parameter  $\beta$  can be set to a large value (8 in the experiments of Section 4) in order to get a rapid state transition in the sigmoids. Finally, following Frangi et al.'s strategy, parameter  $s$  can be set to a percentage of the maximum value of  $S$ . In the experiments of Section 4 we have obtained good results by setting  $s = 0.15 \max(S)$ .

It is important to remark that RPD is robust with respect to uncorrelated noise. This is because this type of noise contributes to the uniform part of the LODG, which is actively disregarded by neglecting the autocorrelation power spectrum of degree 0,  $P_0$ , in parameters  $E$  and  $E_{1/2}$  computed through (11). Furthermore, unlike noise, ring patterns detection is not affected by disregarding  $P_0$ , as already mentioned.

#### 4. Results

Table 1 shows the methods used in the experiments including the newly proposed FST and RPD introduced in Sections 2 and 3, respectively. HF, OOF and SBA have been run at three scales: 0.4, 0.8 and 1.2 mm, whereas RST, FST and RPD have been run at a single scale of 1.2 mm. In order to assess the effect of  $\hat{r}$  on both RST and FST, the factor  $\alpha$  of RST in (5) has been disregarded in our implementation of RST. Apart from  $\alpha$ , standard parameters have been used for all methods. Such parameters have been used since the tested methods have been proposed for similar applications. Implementations provided by the authors have been used for OOF and SBA. The methods have been applied to computed tomography angiography (CTA) datasets provided by the coronary artery stenoses detection and quantification and lumen segmentation in CTA images challenge (Kirişli et al., 2013).

Fig. 8 shows a visual comparison of the results of the measurements for a section located at the beginning of the LCA of dataset 10. As shown in the figure, HF is affected by overshootings that can either create false positives at edges, especially at dark gaps (see the edges at the second and fifth columns) or false negatives (see the holes inside the vessel at the fourth and fifth columns), which is not a problem for the proposed methods. OOF also has problems at the edges and is more sensitive to noise. In turn, RST has problems when the vessels are close to strong structures such as the heart chambers. Thus,

$\alpha$ , which has not been considered in our implementation, has to deal with this problem at a cost of increasing its computational cost. SBA has a good performance, but, similarly to HF, it is prone to overshooting artifacts, mainly due to the use of second order derivatives. FST solves most of the problems faced by other methods, as it is less affected by overshooting artifacts, it is less sensitive to noise and it is less affected by nearby structures. However, FST can still face difficulties with small vessels and bifurcations mainly due to its low order nature. Finally, RPD is not only more consistent but it is also better at delineating the centerline of vessels and bifurcations, which makes it more suitable for centerline tracking and segmentation.

A good vesselness method should give a good contrast between vessels and surrounding tissue. This property is related to discriminability as described in Moreno et al. (2009). This property can be assessed by comparing the mean vesselness inside a generalized cylinder of radius  $\delta_1$  to the one at the region between that cylinder and a larger concentric generalized cylinder (cf. Fig. 9). For this purpose, we generated generalized cylinders by dilating the centerlines of the coronary arteries provided by the challenge (Kirişli et al., 2013), which in turn were computed by applying the centerline extraction method described in Goldenberg et al. (2012). The radius of the outer cylinder has been fixed to 6.8 mm. The mean vesselness inside and outside the inner generalized cylinder are referred to as  $\bar{V}_{in}$  and  $\bar{V}_{out}$  respectively, while the mean vesselness at the centerline is referred to as  $\bar{V}_{cl}$ . Also, the standard deviation at the outside is referred to as  $\sigma_{out}$ .

In order to assess contrast and contrast to noise ratio (CNR), respectively, we have evaluated  $\Psi = (\bar{V}_{in} - \bar{V}_{out})/\bar{V}_{cl}$  and  $\Phi = \Psi/\sigma_{out}$ . Fig. 10 shows the evolution  $\Psi$  and  $\Phi$  with respect to  $\delta_1$  for all methods and 18 datasets. The original images without processing have also been included in the figure as a baseline. The comparison was performed on the direct output of the methods in order to avoid bias related to any post-processing of such outputs. As shown, except OOF, all tested methods are able to improve the contrast from the original image under both  $\Psi$  and  $\Phi$ . FST and RPD have the best performance for  $\Psi$ , which means that these methods yield the best contrast between the vessel and the surroundings. However, RPD yields a much better CNR, measured through  $\Phi$ , than FST. This means that RPD is able to generate fewer artifacts than FST, which is consistent with the visual comparison of Fig. 8. HF has good CNR close to the centerline, but its performance quickly degrades with  $\delta$ , which is caused by the aforementioned overshooting artifacts. The low performance of OOF is mainly due to its noise sensitivity. As shown, RPD and FST outperform SBA and RST respectively.

As already mentioned, vesselness filters can be used in different applications. For example, some vessel segmentation methods rely on preprocessing in which vessels are enhanced before the actual segmentation is performed. In fact, any segmentation method is expected to be improved by performing such a preprocessing. To assess the performance of the methods in this particular application, thresholding, which is the simplest segmentation algorithm, has been applied after filtering. It is important to emphasize that any segmentation method can be used for this assessment due to the fact that our focus is on vessel enhancement rather on vessel segmentation.

**Table 1**  
Methods used in the experiments. FST and RPD are the methods proposed in this paper.

Method	Abbrev.	Type	Scales	Refs.
Frangi et al.'s	HF	Hessian	3	Frangi et al. (1998)
Optimally oriented flux	OOF	Gradient	3	Law and Chung (2008); Law et al. (2012)
Radial structure tensor	RST	Gradient	1	Wiemker et al. (2013)
Structure ball analysis	SBA	2nd order derivatives, spherical harmonics	3	Rivest-Hénault and Cheriet (2013)
Filtered structure tensor	FST	Gradient	1	Eq. (6)
Ring pattern detector	RPD	Gradient, spherical harmonics	1	Eq. (17)

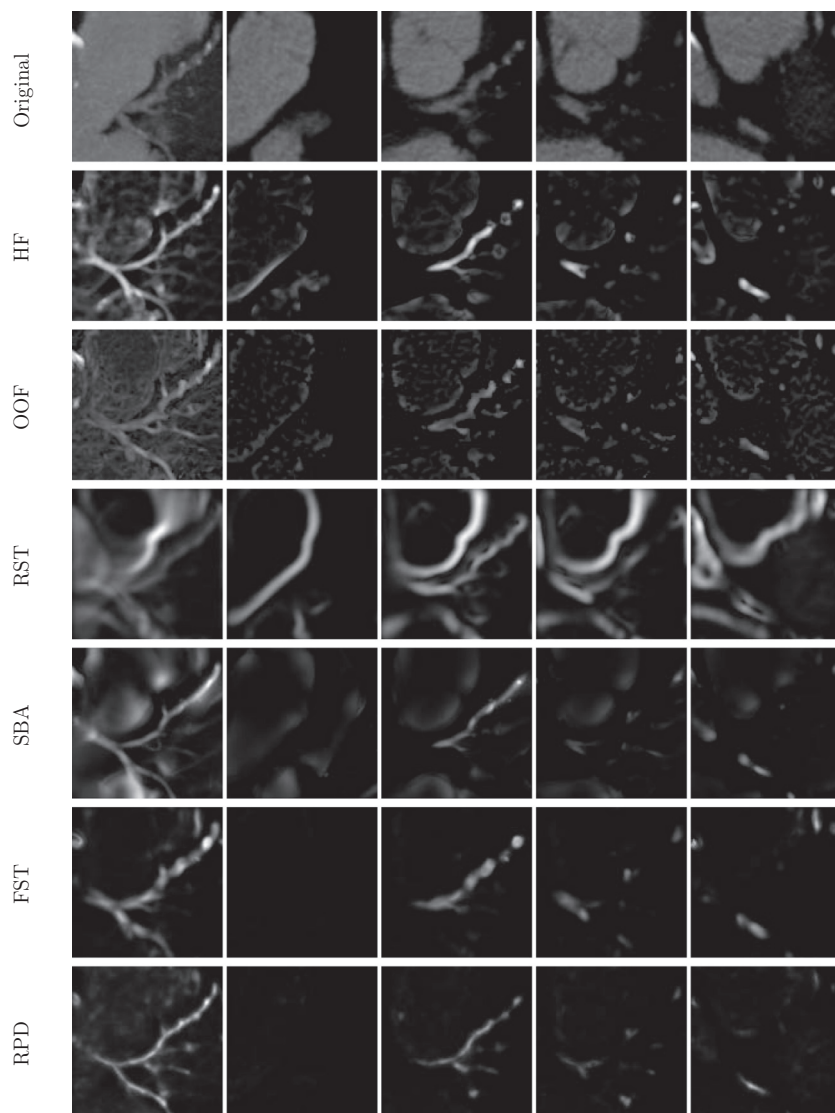


**Fig. 8.** Results with CTA data. First row: CTA data corresponding to the beginning of the LCA of the dataset number 10. Rows 2–7: output of HF, OOF, RST, SBA, FST and RPD, respectively. First column: maximum intensity projection of the CTA and the output of the filters. Columns 2–5: four different slices of the same volume and their corresponding filter outputs.

Considering that the manually annotated ground truth is only available for some coronary arteries (Kirişli et al., 2013), the output of the filters has been resampled through curved multi-planar reconstruction (cMPR) guided by the provided centerlines, and then, slices not belonging to the ground truth have been discarded.

Two different scenarios have been considered. In the first scenario, nearby structures such as the heart chambers are mostly disregarded by discarding segmented data beyond 5 mm from the centerline. In the second scenario, such nearby structures are considered. However, since other structures such as pulmonary vessels must be disregarded, segmented data beyond 9 mm from the centerline have been discarded for the second scenario.

Fig. 11 shows the Dice coefficients obtained with different threshold values after vessel enhancement on dataset 10. As shown, the performance of the original data is fairly good in the first scenario where it is only outperformed by FST, RPD and HF. However, as expected, its performance largely decays in the second scenario, where it is outperformed by all tested methods. The performance of RPD, FST and RST is similar in both cases, which means that they are less affected by artifacts from nearby structures than HF, OOF and SBA. FST yielded the best maximum value in both cases (0.71 and 0.66) followed by RPD

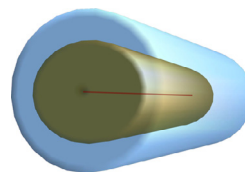


**Fig. 9.** Vesselness inside the inner generalized cylinder is compared with the one at the region between the inner and the outer generalized cylinder. The centerline is depicted in red. (For interpretation of the references to color in this figure legend, the reader is referred to the web version of this article.)

(0.66 and 0.61). On the other hand, RPD is the most stable method with respect to the threshold since it can yield high Dice coefficients for a larger range of thresholds.

The methods were run in a workstation with 6 Intel Xeon CPUs at 2.4 GHz and 24GB of RAM. Regarding computational costs, OOF and HF were the most efficient with 6 and 17 min per examination in average, respectively. Our non-optimized MATLAB implementations of FST and RST took 25 and 28 min per examination, respectively. Finally, SBA and RPD took 335 and 84 min per examination, respectively.



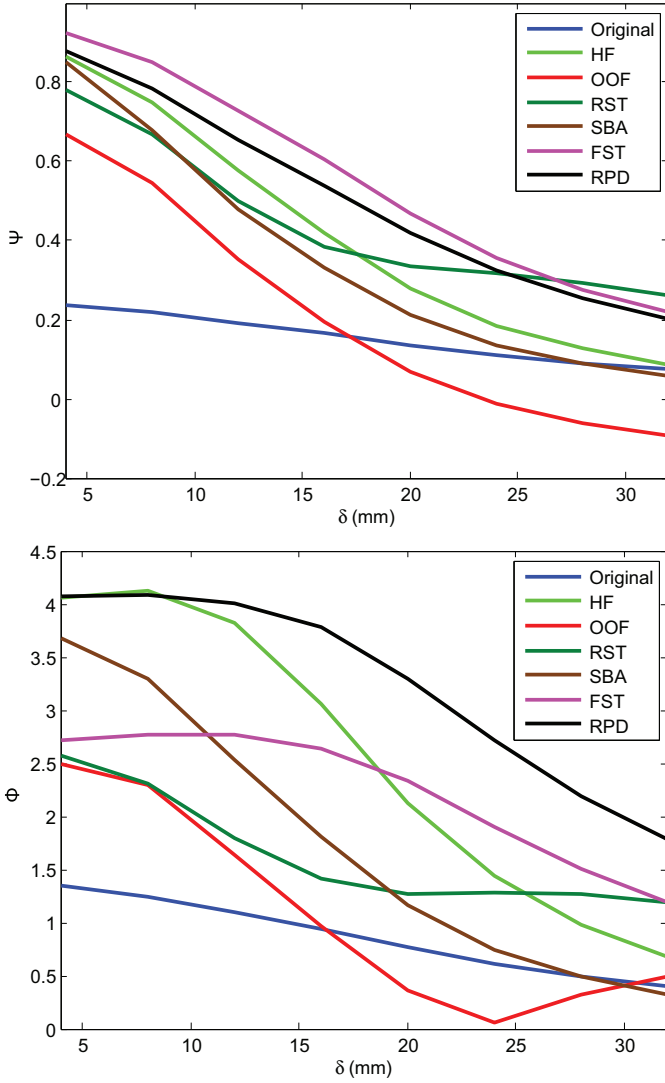


**Fig. 10.** Evolution of  $\Psi$  (top) and  $\Phi$  (bottom) with the distance  $\delta$  from the centerlines of 18 CTA datasets for the tested methods. FST and RPD are the proposed methods.

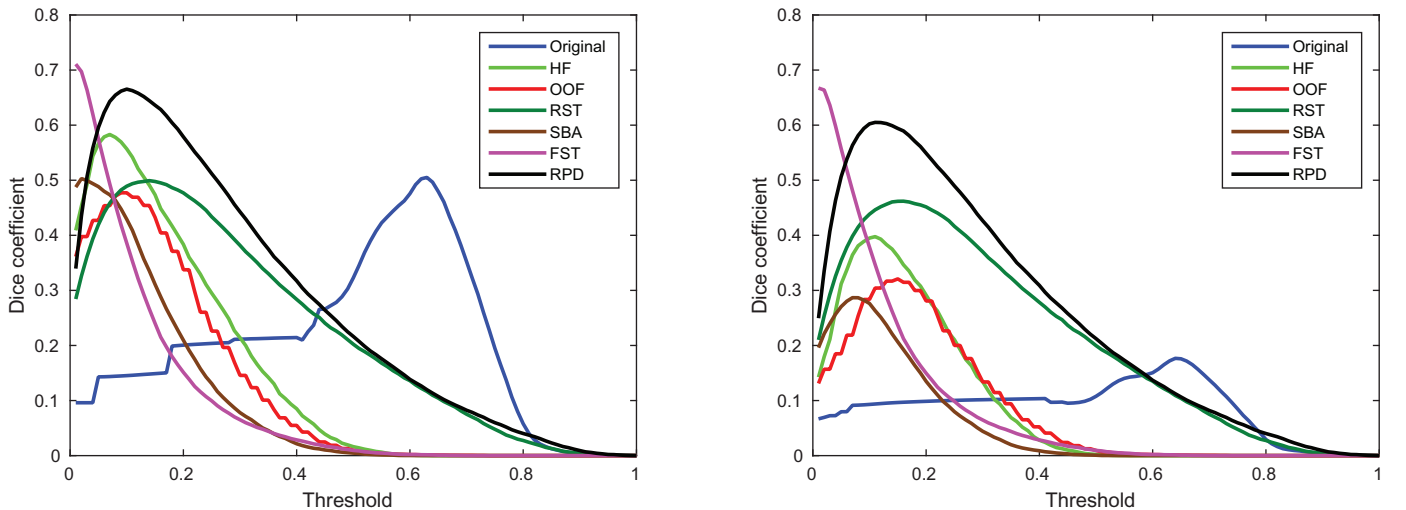


**Fig. 11.** Dice coefficients for segmentations obtained through different thresholds after vessel enhancement with the tested vesselness filters on dataset 10. Left: voxels farther away than 5 mm from the centerline are disregarded. Right: voxels farther away than 9 mm from the centerline are disregarded. Gray-scale values have been normalized to the range  $[0,1]$  before thresholding in all cases. FST and RPD are the proposed methods.

## 5. Discussion

We have introduced a vesselness measure based on the analysis of the LODG in the spherical harmonics domain. The method tackles the drawbacks of the Hessian-based methods by using first order derivatives only. In an intermediate step, a modification of the structure tensor is used to represent the LODG, which effectively tackles the problems of previously proposed structure tensor-based techniques by analyzing the filtered gradient computed through (7). The experimental results with real data are promising, since the proposed methods yield better results than the state-of-the-art with real data.

The proposed method deals with different issues from previous approaches as follows. First, by using the filtered gradient of (7), the filter becomes less sensitive to strong nearby structures, making it more appropriate for applications such as coronary artery imaging. Second, the method is robust with respect to uncorrelated noise. Parameters  $E$  and  $E_{1/2}$  disregard the autocorrelation power spectrum of degree 0, which results in noise rejection while still being sensitive to ring patterns in the LODG. Third, the proposed approach is able to analyze multiple scales by performing the computations at a single scale. Fourth, the filter is scale-invariant, which means that it is able to yield a good response for both large and small vessels. The scale invariance is attained by normalization factors on parameters  $E$ ,  $E_{1/2}$ ,  $U$  and  $U_{1/2}$ , which make the filter insensitive to the strength of the rings, which in turn is related to the size of the vessels. Fifth, the proposed method is able to deal with bifurcations. The filter has been tuned not only for detecting a single ring in the LODG, which is related to the presence of a vessel, but also for detecting two and three rings, which are characteristic in “T” and “Y” bifurcations, respectively. In particular, the method has been optimized for distinguishing LODGs that contain 1–3 rings from other type of distributions that might stem from non-vessel structures. Finally, the filter is rotation-invariant. Thus, the same response will be obtained regardless the orientation of the vessel. This property is given by the rotation invariance of the autocorrelation power spectra, which are used for computing  $E$ ,  $E_{1/2}$ ,  $U$  and  $U_{1/2}$ .

It should be noticed that RST is consistently more expensive than FST, even without the computation of function  $\alpha$  in (5). In turn, RPD is also more efficient than SBA, mainly since the latter requires computations at different scales.

It is important to remark that our current implementations of RST and FST can largely be optimized, so they can become as efficient as

HF and OOF. In turn, it is a fact that methods based on the structure tensor are faster than the ones based on spherical harmonics. One reason of this is that the former can be seen as lower order approximations of the latter. There are different strategies that can be applied in order to reduce the computational effort of techniques based on spherical harmonics. On the one hand, an effective strategy is to reduce the domain by discarding non relevant areas with less expensive methods. For example, since vessels are usually limited to a certain range of diameters, thickness measurements (e.g., the method proposed by Moreno et al. (2012a)) can be used to discard vast regions where the estimated thickness is far from the expected range. With this strategy, the domain can easily be reduced to less than 10% of the voxels. On the other hand, the latest advances in spherical harmonics processing open the door to large improvements with respect to the current implementations of methods such as SBA and RPD. Especially, the advances on efficient parallel schemes (Ambuluri et al., 2013; Szydlarski et al., 2014) and optimal sampling approaches (Khalid et al., 2014) are particularly promising.

Our ongoing work includes using the proposed vesselness measurement for accurate vessel segmentation. Although the focus of this paper is not vessel segmentation, it is worthwhile to mention that the current best Dice coefficient in the lumen segmentation challenge is 0.76 (Lugauer et al., 2014), which means that the 0.71 and 0.66 obtained by applying a simple thresholding after enhancement with FST and RPD respectively on one dataset is encouraging.

## Acknowledgements

We thank Hortense Kirişli, Theo van Walsum and Wiro Niessen for providing the CTA data and centerlines used in the experiments. This research has been supported by the Swedish Research Council (VR), Grants nos. 2014–6153 and 2012–3512, and the Swedish Heart-Lung Foundation (HLF), Grant no. 2011–0376.

## References

- Agam, G., Armato, S., Wu, C., 2005. Vessel tree reconstruction in thoracic CT scans with application to nodule detection. *IEEE Trans. Med. Imag.* 24 (4), 486–499. doi:10.1109/TMI.2005.844167.
- Agam, G., Wu, C., 2005. Probabilistic modeling based vessel enhancement in thoracic CT scans. In: *Proceedings of the Conference on Computer Vision and Pattern Recognition, CVPR*, vol. 2, pp. 649–654. doi:10.1109/CVPR.2005.280.
- Ambuluri, S., Garrido, M., Caffarena, G., Ogniewski, J., Ragnemalm, I., 2013. New radix-2 and radix-2<sup>2</sup> constant geometry fast Fourier transform algorithms for GPUs. In: *Proceedings of the Conference on CGVCVP*, pp. 59–66.
- Armande, N., Montesinos, P., Monga, O., 1996. A 3D thin nets extraction method for medical imaging. In: *Proceedings of the International Conference on Pattern Recognition, ICPR*, vol. 1, pp. 642–646. doi:10.1109/ICPR.1996.546103.
- Auvray, V., Jandt, U., Florent, R., Schäfer, D., 2009. Improved vessel enhancement for fully automatic coronary modeling. In: *Proc. SPIE*, 7259 72592B–72592B–8, doi:10.1117/12.810144.
- Bauer, C., Bischof, H., 2008. A novel approach for detection of tubular objects and its application to medical image analysis. In: *Proceedings of the Conference on DAGM*. In: *LNCs*, vol. 5096. Springer Berlin Heidelberg, pp. 163–172. doi:10.1007/978-3-540-69321-5\_17.
- Benmansour, F., Cohen, L.D., 2011. Tubular structure segmentation based on minimal path method and anisotropic enhancement. *Int. J. Comput. Vis.* 92 (2), 192–210. doi:10.1007/s11263-010-0331-0.
- Cañero, C., Radeva, P., 2003. Vesselness enhancement diffusion. *Pattern Recognit. Lett.* 24 (16), 3141–3151. <http://dx.doi.org/10.1016/j.patrec.2003.08.001>.
- Cetin, S., Demir, A., Yezzi, A., Degertekin, M., Unal, G., 2013. Vessel tractography using an intensity based tensor model with branch detection. *IEEE Trans. Med. Imag.* 32 (2), 348–363. doi:10.1109/TMI.2012.2227118.
- Dong, Q., Schoenberg, S.O., Carlos, R.C., Neimatallah, M., Cho, K.J., Williams, D.M., Kazanjian, S.N., Prince, M.R., 1999. Diagnosis of renal vascular disease with MR angiography. *Radiographics* 19 (6), 1535–1554. doi:10.1148/radiographics.19.6.g99no041535.
- Edvardson, H., Smedby, Ö., 2003. Compact and efficient 3D shape description through radial function approximation. *Comput. Methods Progr. Biomed.* 72 (2), 89–97. <http://dx.doi.org/10.1016/S0169-2607(02)00126-8>.
- Förstner, W., 1986. A feature based correspondence algorithm for image matching. In: *Int. Arch. Photogramm. Remote Sens.* 26, pp. 150–166.
- Frangi, A., Niessen, W., Vincken, K., Viergever, M., 1998. Multiscale vessel enhancement filtering. In: *Proceedings of the Conference on MICCAI*, pp. 130–137. doi:10.1007/BFb0056195.
- Friman, O., Hindennach, M., Kühnel, C., Peitgen, H.-O., 2010. Multiple hypothesis template tracking of small 3D vessel structures. *Med. Image Anal.* 14 (2), 160–171. doi:10.1016/j.media.2009.12.003.
- Goldenberg, D., Eilott, G., Begelman, abd E. Ben-Ishai, E.W., Peled, N., 2012. Computer-aided simple triage (CAST) for coronary CT angiography (CCTA). *Int. J. Comput. Assist. Radiol. Surg.* 7 (6), 819–827. doi:10.1007/s11548-012-0684-7.
- Hannink, J., Duijs, R., Bekkers, E.J., 2014. Vesselness via multiple scale orientation scores. *CoRR* abs/1402.4963. <http://arxiv.org/abs/1402.4963>.
- Hernández Hoyos, M., Orlowski, P., Piatkowska-Janko, E., Bogorodzki, P., Orkisz, M., 2006. Vascular centerline extraction in 3D MR angiograms for phase contrast MRI blood flow measurement. *Int. J. Comput. Assist. Radiol. Surg.* 1 (1), 51–61. doi:10.1007/s11548-006-0005-0.
- Hogg, K., Brown, G., Dunning, J., Wright, J., Carley, S., Foex, B., Mackway-Jones, K., 2006. Diagnosis of pulmonary embolism with ct pulmonary angiography: a systematic review. *Emerg. Med. J.* 23 (3), 172–178. doi:10.1136/emj.2005.029397.
- Horn, B.K.P., 1984. Extended Gaussian images. *Proc. IEEE* 72 (12), 1671–1686. doi:10.1109/PROC.1984.13073.
- Khalid, Z., Kennedy, R., McEwen, J., 2014. An optimal-dimensionality sampling scheme on the sphere with fast spherical harmonic transforms. *IEEE Trans. Signal Process.* 62 (17), 4597–4610. doi:10.1109/TSP.2014.2337278.
- Kirbas, C., Quek, F., 2004. A review of vessel extraction techniques and algorithms. *ACM Comput. Surv.* 36 (2), 81–121. doi:10.1145/1031120.1031121.
- Kirişli, H., Schaap, M., Metz, C., Dharampal, A., Meijboom, W., Papadopolou, S., Dedic, A., Nieman, K., de Graaf, M., Meijjs, M., Cramer, M., Broersen, A., Cetin, S., Eslami, A., Flórez-Valencia, L., Lor, K., Matuszewski, B., Melki, I., Mohr, B., Öksüz, I., Shahzad, R., Wang, C., Kitslaar, P., Unal, G., Katouzian, A., Orkisz, M., Chen, C., Precioso, F., Najman, L., Masood, S., Ünay, D., van Vliet, L., Moreno, R., Goldenberg, R., Vucini, E., Krestin, G., Niessen, W., van Walsum, T., 2013. Standardized evaluation framework for evaluating coronary artery stenosis detection, stenosis quantification and lumen segmentation algorithms in computed tomography angiography. *Med. Image Anal.* 17 (8), 859–876. doi:10.1016/j.media.2013.05.007.
- Krisian, K., 2002. Flux-based anisotropic diffusion applied to enhancement of 3-D angiogram. *IEEE Trans. Med. Imag.* 21 (11), 1440–1442. doi:10.1109/TMI.2002.806403.
- Law, M., Chung, A., 2009. Efficient implementation for spherical flux computation and its application to vascular segmentation. *IEEE Trans. Image Process.* 18 (3), 596–612. doi:10.1109/TIP.2008.2010073.
- Law, M.W., Chung, A.C., 2008. Three dimensional curvilinear structure detection using optimally oriented flux. In: *Proceedings of the European Conference on Computer Vision ECCV*, pp. 368–382. doi:10.1007/978-3-540-88693-8\_27.
- Law, M.W., Tay, K., Leung, A., Garvin, G.J., Li, S., 2012. Dilated divergence based scale-space representation for curve analysis. In: *Proceedings of the European Conference on Computer Vision ECCV*, pp. 557–571. doi:10.1007/978-3-642-33709-3\_40.
- Law, M.W.K., Tay, K., Leung, A., J Garvin, G., Li, S., 2013. Intervertebral disc segmentation in MR images using anisotropic oriented flux. *Med. Image Anal.* 17 (1), 43–61. doi:10.1016/j.media.2012.06.006.
- Lesage, D., Angelini, E.D., Bloch, I., Funka-Lea, G., 2009. A review of 3D vessel lumen segmentation techniques: Models, features and extraction schemes. *Med. Image Anal.* 13 (6), 819–845. doi:10.1016/j.media.2009.07.011.
- Li, Q., Sone, S., Doi, K., 2003. Selective enhancement filters for nodules, vessels, and airway walls in 2- and 3-dimensional CT scans. *Med. Phys.* 30 (8), 2040–2051. doi:10.1118/1.1581411.
- Lugauer, F., Zheng, Y., Hornegger, J., Kelm, B., 2014. Precise lumen segmentation in coronary computed tomography angiography. In: *Medical Computer Vision: Algorithms for Big Data*. Springer, pp. 137–147. doi:10.1007/978-3-319-13972-2\_13.
- Manniesing, R., Viergever, M.A., Niessen, W.J., 2006. Vessel enhancing diffusion: a scale space representation of vessel structures. *Med. Image Anal.* 10 (6), 815–825. doi:10.1016/j.media.2006.06.003.
- Marwan, M., Hausleiter, J., Abbasa, S., Hoffmann, U., Becker, C., Ovrehus, K., Ropers, D., Bathina, R., Berman, D., Anders, K., Uder, M., Meave, A., Alexanderson, E., Achenbach, S., 2014. Multicenter evaluation of coronary dual-source CT angiography in patients with intermediate risk of coronary artery stenoses (MEDIC): study design and rationale. *J. Cardiovasc. Comput. Tomogr.* 8 (3), 183–188. doi:10.1016/j.jcct.2014.04.006.
- Moreno, R., Borga, M., Smedby, Ö., 2012a. Estimation of trabecular thickness in grayscale images through granulometric analysis. In: *Proc. SPIE Med. Imag. Image Process.* 8314, pp. 831451–1–831451–9. doi:10.1117/12.906734.
- Moreno, R., Borga, M., Smedby, Ö., 2012b. Generalizing the mean intercept length tensor for gray-level images. *Med. Phys.* 39 (7), 4599–4612. doi:10.1118/1.4730502.
- Moreno, R., Puig, D., Julià, C., Garcia, M.A., 2009. A new methodology for evaluation of edge detectors. In: *Proceedings of the International Conference on Image Processing ICIP*, pp. 2157–2160. doi:10.1109/ICIP.2009.5414086.
- Mos, I.C.M., Klok, F.A., Kroft, L.J.M., de Roos, A., Dekkers, O.M., Huisman, M.V., 2009. Safety of ruling out acute pulmonary embolism by normal computed tomography pulmonary angiography in patients with an indication for computed tomography: systematic review and meta-analysis. *J. Thromb. Haemost.* 7 (9), 1491–1498. doi:10.1111/j.1538-7836.2009.03518.x.
- Nemitz, O., Rumpf, M., Tasdizen, T., Whitaker, R., 2007. Anisotropic curvature motion for structure enhancing smoothing of 3D MR angiography data. *J. Math. Imaging Vis.* 27 (3), 217–229. doi:10.1007/s10851-006-0645-2.
- Özarslan, E., Mareci, T.H., 2003. Generalized diffusion tensor imaging and analytical relationships between diffusion tensor imaging and high angular resolution diffusion imaging. *Magn. Res. Med.* 50 (5), 955–965. doi:10.1002/mrm.10596.
- Parker, D.L., Tsuruda, J.S., Goodrich, K.C., Alexander, A.L., Buswell, H.R., 1998. Contrast-enhanced magnetic resonance angiography of cerebral arteries: a review. *Invest. Radiol.* 33 (9), 560–572.

- Prince, M., Grist, T., Debatin, J., 1999. *3D Contrast MR Angiography*. Springer, Berlin.
- Prinet, V., Monga, O., Ge, C., Xie, S., Ma, S., 1996. Thin network extraction in 3D images: application to medical angiograms. In: *Proceedings of the International Conference on Pattern Recognition ICPR*, vol. 3, pp. 386–390. doi:[10.1109/ICPR.1996.546975](https://doi.org/10.1109/ICPR.1996.546975).
- Qian, X., Brennan, M.P., Dione, D.P., Dobrucki, W.L., Jackowski, M.P., Breuer, C.K., Sinusas, A.J., Papademetris, X., 2009. A non-parametric vessel detection method for complex vascular structures. *Med. Image Anal.* 13 (1), 49–61. doi:[10.1016/j.media.2008.05.005](https://doi.org/10.1016/j.media.2008.05.005).
- Rivest-Hénault, D., Cheriet, M., 2013. 3-D curvilinear structure detection filter via structure-ball analysis. *IEEE Trans. Image Process.* 22 (7), 2849–2863. doi:[10.1109/TIP.2013.2240005](https://doi.org/10.1109/TIP.2013.2240005).
- Rudyanto, R.D., Kerkstra, S., van Rikxoort, E.M., Fetita, C., Brillet, P.-Y., Lefevre, C., Xue, W., Zhu, X., Liang, J., Ökstüz, İ., Ünay, D., Kadipaşaoğlu, K., San José Estépar, R., Ross, J.C., Washko, G.R., Prieto, J.-C., Hernández Hoyos, M., Orkisz, M., Meine, H., Hüllebrand, M., Stöcker, C., Lopez Mir, F., Naranjo, V., Villanueva, E., Staring, M., Xiao, C., Stael, B.C., Fabijanska, A., Smistad, E., Elster, A.C., Lindseth, F., Foruzan, A.H., Kiros, R., Popuri, K., Cobzas, D., Jimenez-Carretero, D., Santos, A., Ledesma-Carbayo, M.J., Helmberger, M., Urschler, M., Pienn, M., Bosboom, D.G., Campo, A., Prokop, M., de Jong, P.A., de Solorzano, C.O., Muñoz-Barrutia, A., van Ginneken, B., 2014. Comparing algorithms for automated vessel segmentation in computed tomography scans of the lung: the VESSEL12 study. *Med. Image Anal.* 18 (7), 1217–1232. doi:[10.1016/j.media.2014.07.003](https://doi.org/10.1016/j.media.2014.07.003).
- Sato, Y., Nakajima, S., Shiraga, N., Atsumi, H., Yoshida, S., Koller, T., Gerig, G., Kikinis, R., 1998. Three-dimensional multi-scale line filter for segmentation and visualization of curvilinear structures in medical images. *Med. Image Anal.* 2 (2), 143–168. doi:[10.1016/S1361-8415\(98\)80009-1](https://doi.org/10.1016/S1361-8415(98)80009-1).
- Schaap, M., Metz, C.T., van Walsum, T., van der Giessen, A.G., Weustink, A.C., Mollet, N.R., Bauer, C., Bogunović, H., Castro, C., Deng, X., Dikici, E., O'Donnell, T., Frenay, M., Friman, O., Hernández Hoyos, M., Kitslaar, P.H., Krissian, K., Kühnel, C., Luengo-Oroz, M.A., Orkisz, M., Smedby, Ö., Styner, M., Szymczak, A., Tek, H., Wang, C., Warfield, S.K., Zambal, S., Zhang, Y., Krestin, G.P., Niessen, W.J., 2009. Standardized evaluation methodology and reference database for evaluating coronary artery centerline extraction algorithms. *Med. Image Anal.* 13 (5), 701–714. doi:[10.1016/j.media.2009.06.003](https://doi.org/10.1016/j.media.2009.06.003).
- Szydlarski, M., Esterie, P., Falcou, J., Grigori, L., Stompör, R., 2014. Parallel spherical harmonic transforms on heterogeneous architectures (graphics processing units/multi-core CPUs). *Concurr. Comput. Pract. Exp.* 26 (3), 683–711. doi:[10.1002/cpe.3038](https://doi.org/10.1002/cpe.3038).
- Vasilevskiy, A., Siddiqi, K., 2002. Flux maximizing geometric flows. *IEEE Trans. Pattern Anal. Mach. Intell.* 24 (12), 1565–1578. doi:[10.1109/TPAMI.2002.1114849](https://doi.org/10.1109/TPAMI.2002.1114849).
- Weustink, A., de Feyter, P., 2011. The role of multi-slice computed tomography in stable angina management: a current perspective. *Neth. Heart J.* 19 (8), 336–343. doi:[10.1007/s12471-011-0096-2](https://doi.org/10.1007/s12471-011-0096-2).
- Wiemker, R., Klinder, T., Bergholdt, M., Meetz, K., Carlsen, I., Bülow, T., 2013. A radial structure tensor and its use for shape-encoding medical visualization of tubular and nodular structures. *IEEE Trans. Vis. Comput. Graph.* 19 (3), 353–366. doi:[10.1109/TVCG.2012.136](https://doi.org/10.1109/TVCG.2012.136).
- Wörz, S., Rohr, K., 2007. Segmentation and quantification of human vessels using a 3-D cylindrical intensity model. *IEEE Trans. Image. Proc.* 16 (8), 1994–2004. doi:[10.1109/TIP.2007.901204](https://doi.org/10.1109/TIP.2007.901204).
- Xiao, C., Staring, M., Shamonin, D., Reiber, J., Stolk, J., Stael, B., 2011. A strain energy filter for 3D vessel enhancement with application to pulmonary CT images. *Med. Image Anal.* 15 (1), 112–124. doi:[10.1016/j.media.2010.08.003](https://doi.org/10.1016/j.media.2010.08.003).
- Xiao, C., Staring, M., Wang, Y., Shamonin, D., Stael, B., 2013. Multiscale bi-Gaussian filter for adjacent curvilinear structures detection with application to vasculature images. *IEEE Trans. Image Proc.* 22 (1), 174–188. doi:[10.1109/TIP.2012.2216277](https://doi.org/10.1109/TIP.2012.2216277).
- Xu, C., Prince, J., 1998. Snakes, shapes, and gradient vector flow. *IEEE Trans. Image Process.* 7 (3), 359–369. doi:[10.1109/83.661186](https://doi.org/10.1109/83.661186).
- Yang, G., Kitslaar, P., Frenay, M., Broersen, A., Boogers, M., Bax, J., Reiber, J., Dijkstra, J., 2012. Automatic centerline extraction of coronary arteries in coronary computed tomographic angiography. *Int. J. Cardiovasc. Imaging* 28 (4), 921–933. doi:[10.1007/s10554-011-9894-2](https://doi.org/10.1007/s10554-011-9894-2).
- Yang, J., Ma, S., Sun, Q., Tan, W., Xu, M., Chen, N., Zhao, D., 2014. Improved Hessian multiscale enhancement filter. *J. Biomed. Mater. Eng.* 24 (6), 3267–3275. doi:[10.3233/BME-141149](https://doi.org/10.3233/BME-141149).
- Zheng, Y., Loziczonek, M., Georgescu, B., Zhou, S.K., Vega-Higuera, F., Comaniciu, D., 2011. Machine learning based vesselness measurement for coronary artery segmentation in cardiac CT volumes. In: *Proc. SPIE*, 7962 doi:[10.1117/12.877233](https://doi.org/10.1117/12.877233), 79621K–79621K–12.
- Zheng, Y., Shen, J., Tek, H., Funka-Lea, G., 2012. Model-driven centerline extraction for severely occluded major coronary arteries. In: *Proceedings of the Conference on MLMI*. Springer, pp. 10–18. doi:[10.1007/978-3-642-35428-1\\_2](https://doi.org/10.1007/978-3-642-35428-1_2).